SCIENTIFIC REPORTS
nature research

Check for updates

OPEN

Strain modulation of TaO_4 planarity in tantalates ultrathin films: surface states engineering

Guilherme Ribeiro Portugal[1,2] & Jeverson Teodoro Arantes[1,2] ✉

Ultrathin films of perovskites have attracted considerable attention once they fit in numerous applications. Over the years, controlling and tuning their properties have been attainable when biaxial strain is applied. Through *ab initio* DFT calculations, (110) ultrathin (Na,K)TaO_3 films were submitted to biaxial tensile and compressive strain. Intrinsically, surface Ta shallow states emerge into the bandgap since the (110) cleavage breaks its octahedral symmetry to create TaO_4 units. Removal of ligands along the *x*-*y* plane stabilizes $d_{x^2-y^2}$ orbitals, which decrease in energy due to lower electrostatic repulsion. Such stabilization is maximized when biaxial tensile increases the TaO_4 planarity towards a square planar symmetry. Accordingly, the corresponding electronic levels move further into the bandgap. Conversely, compressive biaxial strain intensifies electrostatic repulsion, closing the TaO_4 tetrahedra, and surface states move to higher energy zones. The reported strain-driven modulation might be applied in different applications, as photocatalysis, ferroelectricity, and spintronics.

ABO_3 perovskite structures have been broadly studied over the last decades, mostly because they constitute a family of oxides widely found in solid-state inorganic chemistry, but also because they fit into numerous technological applications[1–3]. Due to their compositional flexibility, cleaving or growing an ABO_3 crystal in different crystallographic directions gives rise to surface planes that have atomic terminations of varying stoichiometry. Accordingly, a whole range of particular electronic structures might be found, which will govern highly sensitive local properties[4]. As a matter of fact, crystal facet engineering has been essential for the controlled improvement of physical and chemical properties, especially in nanostructures[5]. In catalytic processes, one of the main fields for perovskite applications, facet selectivity has been greatly investigated as it directly affects the efficiency of nanostructured catalysts[6,7].

In an ideal perovskite, a cubic lattice is composed of a corner-sharing BO_6 octahedra framework whose dodecahedral interspaces are filled with A-site cations. Breaking such crystal will eventually expose lower coordination $BO_{x=3,4,5}$ units on the surface, which is the major responsible for the electronic structure of cleaved crystals. Much is known about how BO_6 octahedra rotation and tilting affect the material's properties[8–10], sometimes inducing particular features as ferroelectricity[11]. However, accurate information regarding other BO_x units is necessary to a complete understanding of physical and electronic properties of perovskites' surfaces.

Of particular interest, meaningful properties have been attributed to BO_4 groups. Molybdates having MoO_4 units presented enhanced O_2 evolution activity, which means their valence bands (VB) are well-aligned with water oxidation potentials[12]. Recently, (100) $NaTaO_3$ orthorhombic slabs have also shown similar alignment thanks to localized TaO_4 energy states[13]. Interestingly, there is strong evidence that the excited energy is localized in isolated BO_4 tetrahedra inside scheelite structures[12]. In sillenites, specific transmittance and absorption peaks in the visible region have been observed and associated with discrete BO_4 groups[14]. Furthermore, in mullite-type $Bi_2B_4O_9$ ($B = Al^{3+}$, Ga^{3+}) materials, unbalanced Mulliken charges and symmetry breaking related to BO_4 tetrahedra assisted the charge separation positively, increasing their photocatalytic reactivity[15]. Although there are a few records of straight relationships between the BO_4 units and electronic structure, further investigation on how its possible configurational geometry might influence the material's electronic properties is required so that their modulation can be feasible.

Among recurrently synthesized nanostructures, thin and ultrathin films allow fine surface science investigations since they have approaching bulk-like characteristics[16]. Such nanostructured materials may have their

[1]Center for Engineering, Modeling and Applied Social Science (CECS), Federal University of ABC (UFABC), Santo André, São Paulo, Brazil. [2]These authors contributed equally: Guilherme Ribeiro Portugal and Jeverson Teodoro Arantes. ✉e-mail: jeverson.teodoro@ufabc.edu.br

properties tuned and controlled when strain (stress) is induced[17,18]. The effects of biaxial strain have been frequently explored due to the surprising responses obtained when it comes to properties' modulation, which ranges from induction of dielectric anomalies[19] to bandgap engineering[20]. To control the amount of induced strain, substrates with different mismatches with the films are usually employed[21]. The application of an electric field to a piezoelectric substrate has also been used to induce biaxial strain and modulate specific properties[22]. Additionally, developed synthesis methodologies have granted refined control of surface particle size as well as surface area and morphology in thin films, not to mention the fact that characterization techniques that are usually difficult to be implemented for nanoparticles (scanning probe microscopy, for instance) can be readily used in 2-D materials[23,24]. Therefore, studying the influence of surface BO_x arrangements on ultrathin films should provide clear evidence of their role in controlling electronic properties.

Recently, several experimental reports have driven their attention to the synthesis of ABO_3 thin films, such as $NaTaO_3$[24,25] and $KTaO_3$[26–28], on different substrates and heterostructures. Amazingly, angstroms-thick perovskites ultrathin films have already been achieved[29–32], which supports reliable theoretical and experimental comparisons. Furthermore, the modulation of perovskite properties by means of biaxial strain is also widely reported and highly relevant to various applications. Magnetic, electrical, and transport properties, for example, react significantly to strain and can therefore be tuned[33,34]. Strain-induced lattice deformation (octahedral tilting)[35] as well as photoluminescence features[36] have also shown considerable changes upon biaxial strain. Here, through *ab initio* density functional theory[37,38], we have systematically studied the effects of biaxial strain on (110) cubic (Na,K) TaO_3 ultrathin films, emphasizing how the geometric arrangement of surface-exposed TaO_4 tetrahedra influence their electronic structure. Shallow surface states of Ta e_g orbitals are located below the conduction band (CB) and can be pushed either into or out of the bandgap as strain is applied and TaO_4 planarity varies. Biaxial tensile strain increases Ta-O bond distances and the unit planarity, stabilizing e_g orbitals and shifting surface states into the gap. The opposite movement is produced when biaxial compressive strain reduces Ta-O bond distances and makes TaO_4 units less planar. To the best of our knowledge, the aforesaid structural-electronic connection has not been reported hitherto and allows bandgap states engineering, which is desirable in many different fields.

Computational Details

Our calculations have run on Vienna Ab Initio Simulation Package (VASP)[39,40], with electron-ion interactions described by projector augmented-wave (PAW)[41] pseudopotentials. For electrons exchange-correlation interactions, the generalized gradient approximation (GGA) within the PBE functional[42] has been used. To sample the Brillouin zone, **k**-points meshes were generated following the Monkhorst-Pack[43] scheme. During geometry optimizations, plane-wave cutoff energy of 520 eV and electronic energy convergence for self-consistent iterations of 10^{-8} eV were set, aiming at accurate results.

In order to have a reference from which ultrathin films could be built using a slab approach, we have first optimized $KTaO_3$ (KTO) and $NaTaO_3$ (NTO) cubic $Pm\bar{3}m$ bulk structures, performing $11 \times 11 \times 11$ **k**-points integrations. The equilibrium lattice parameters were $a_0^{KTO} = 4.04$ Å and $a_0^{NTO} = 3.98$ Å, which are in agreement with experimentally reported values[44,45]. Typical semiconductor band structures (Fig. 1S) with a Γ-R indirect bandgap of 2.07 eV (KTO) and 2.26 eV (NTO) have been obtained. Despite being well-known that GGA underestimates the bandgap when compared to experimental data[45,46], it agrees with other similar theoretical studies[47,48].

Ultrathin KTO and NTO films were constructed by replicating the bulk and cleaving it in the (110) direction. Thus, 12 layers thick (~31 Å) films that expose such a surface were relaxed with a 15 Å vacuum to minimize image self-interactions from periodic boundary conditions. The **k**-points integration was performed up to a $5 \times 1 \times 5$ grid. To simulate in-plane epitaxial strain, the interplane *x*-*z* lattice constants were changed up to −4% and 4% for compressive and tensile strain, respectively. We designated the strain as $\sigma = [(\alpha_{KTO,NTO} - a_0)/a_0] \times 100$, where $\alpha_{KTO,NTO}$ is the strained lattice parameter and a_0 is the bulk optimized lattice parameter.

Results and Discussion

According to the equilibrium structure of the films, biaxial strain may induce changes in both structural (bond angles, bond distances, crystallinity, etc.) and electronic properties (bandgap, electronic states, Fermi level, etc.). Strain-free, tensile $\sigma = 4\%$ ($\alpha_{KTO} = 4.02$ Å, $\alpha_{NTO} = 4.14$ Å), and compression $\sigma = -4\%$ ($\alpha_{KTO} = 3.88$ Å, $\alpha_{NTO} = 3.82$ Å) converged structures are displayed in Fig. 1. For both KTO and NTO, strain-free films are more stable than those under tensile and compressive strain (Fig. 2S). Despite exposing polar terminations with non-zero formal charges, no surface reconstruction has been observed. Therefore, an electronic reconstruction mechanism will compensate the polarity induced by the cleavage. KTO structures retain their cubic lattice and relaxation occurs by changes in the interlayer spacing along the *y*-axis. NTO films, in turn, relax by similar mechanisms but also allow the rotation of internal TaO_6 and surface TaO_4 units. Note that under biaxial compression, the film acquires a more orthorhombic character while the bulk cubic group spacing can be partially recovered under tensile. A closer look at surface layers reveals a common feature presented by both films upon relaxation. Under biaxial compression ($\sigma < 0\%$), Ta-O bond distances decrease and TaO_4 tetrahedral units become less planar, whereas under biaxial tensile strain ($\sigma > 0\%$), Ta-O bond distances increase and so does their planarity. We here call planarity (P_L) an average of in-plane O-Ta-O angles so that the upper planarity limit corresponds to both *x* and *z* plane angles being 180°.

Since surface states are crucial in the electronic structure of low dimension materials, we have plotted the projected density of states on the potassium (K) *s*, oxygen (O) *p*, and tantalum (Ta) *d* orbitals in Fig. 2. As in bulk, the valence band maximum consists of O 2*p* states and the conduction band minimum is mostly Ta 5*d* levels with a slight O 2*p* contribution, which indicates *d*-*p* (π) hybridization states. Nevertheless, a metallic character is observed in all films as a consequence of their polarity, which induces electronic reconstruction by filling up conduction states. It is interesting to note that there are spin up well-localized energy states near the CB which appear to be shallow

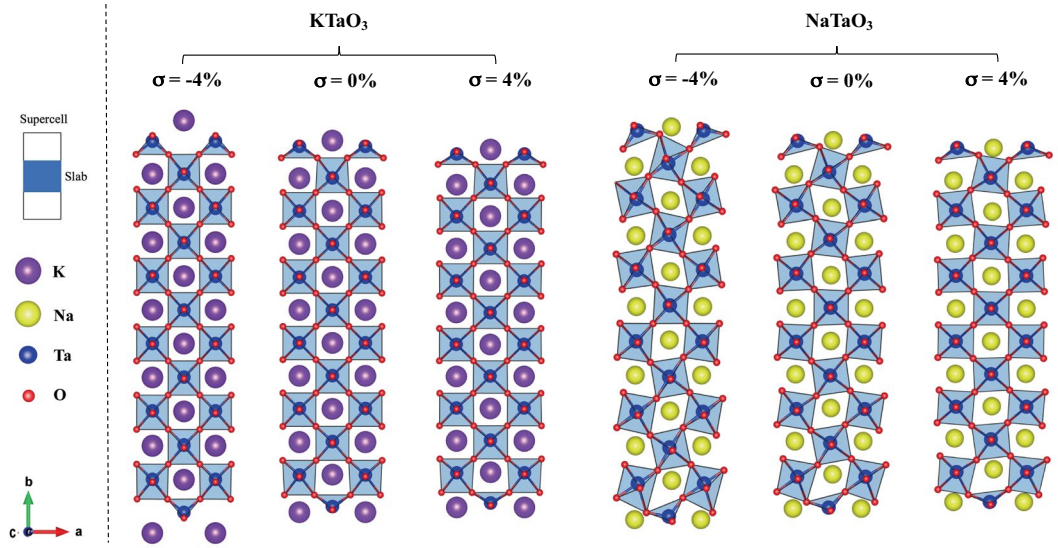

Figure 1. Optimized structures of ultrathin KTO (left panel) and NTO (right panel) films. For each film, the structure having the bulk lattice constant ($\sigma = 0\%$) is in the center, whereas the maximum compression ($\sigma = -4\%$) is on the left, and the maximum tensile ($\sigma = 4\%$) is on the right. In both cases, surface TaO_4 tetrahedra become more planar under biaxial tensile and less planar under biaxial compressive strain.

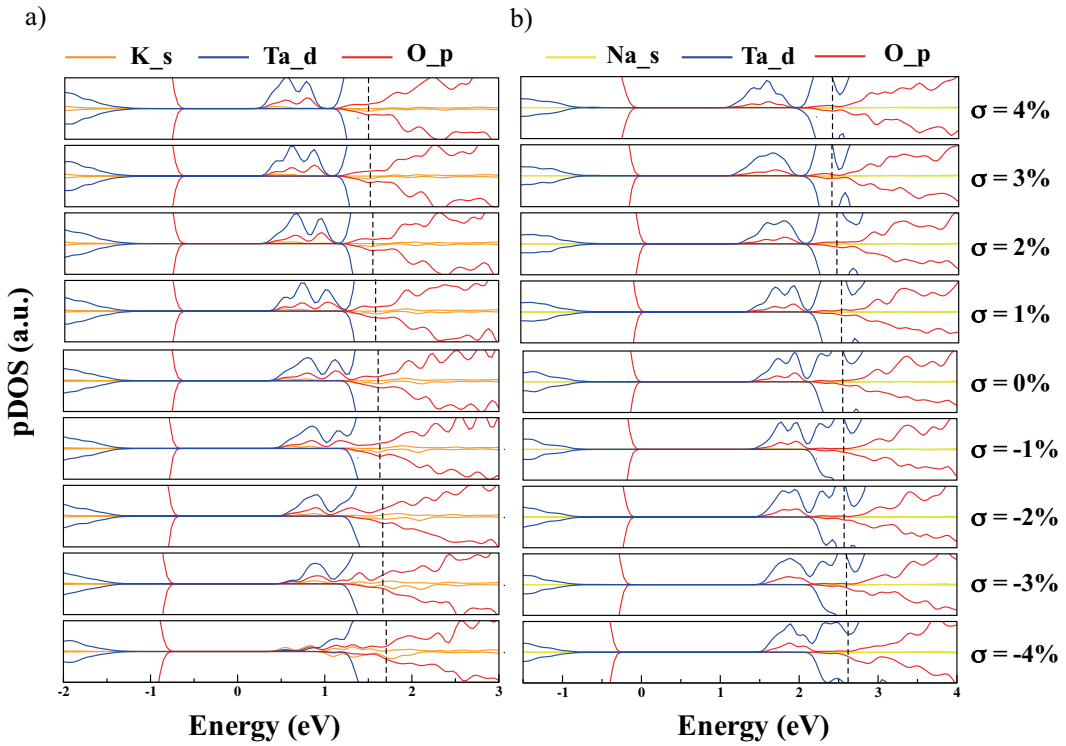

Figure 2. Projected density of states of KTO (**a**) and NTO (**b**) ultrathin films. Surface states are clearly seen near the conduction band bottom of the films. When compression is induced, $\sigma < 0\%$, such levels are pushed towards the conduction band. Oppositely, when tensile is applied, $\sigma > 0\%$, they move into the bandgap. Black dashed lines represent the Fermi levels, and the plots were aligned according to their electrostatic potential.

and within the bandgap, especially under tensile. The layer resolved projected density of states (LRPDOS, Fig. 3S) confirms that such states are derived from surface TaO_4 units. Under compressive conditions where $\sigma < 0\%$, these states migrate to higher energy regions, eventually entering the CB energy zones. When tensile acts on the system, $\sigma > 0\%$, the opposite behavior is observed and they move to lower energy zones within the material's bandgap.

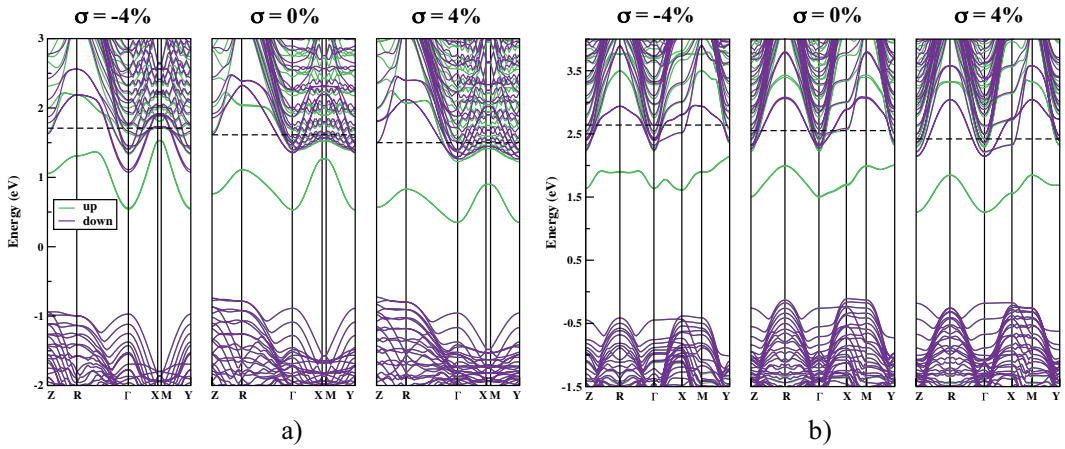

Figure 3. Band structure of KTO (**a**) and NTO (**b**) ultrathin films. In each panel, the strain-free case is in the middle, maximum compression is on the left, and maximum tensile in on the right. Surface up states near the CB are confirmed and their change when $\sigma \neq 0\%$ is evident. Black dashed lines represent the Fermi levels, and the plots were aligned according to their electrostatic potential.

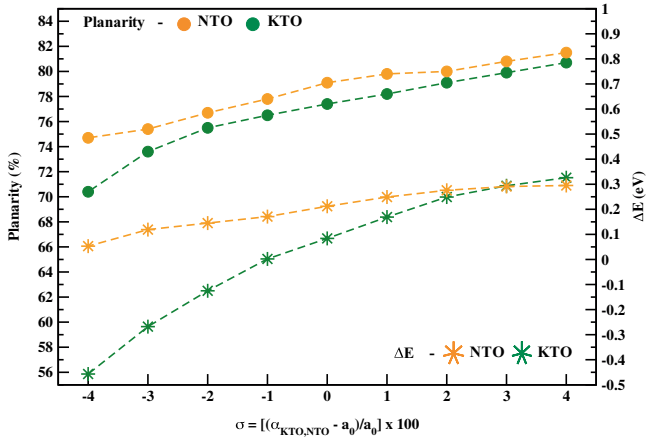

Figure 4. Surface TaO_4 planarity (P_L) and the energy difference between shallow Ta surface states and the CB (ΔE) as functions of biaxial strain (σ). On the left y-axis, P_L (bullets) behaves almost linearly with strain and, intrinsically, NTO has surface TaO_4 units more planar than KTO ones. On the right y-axis, ΔE (stars) increases up to a limit around 0.30 eV. Negative values of ΔE indicate surface states/CB overlap.

The band structure of the films (Fig. 3) helps in describing such TaO_4 surface states, pointing out their energy difference (ΔE) regarding the CB. A complete plot of both P_L and ΔE as functions of σ can be seen in Fig. 4 (all the related data is in Table 1S). It turns out that for $\sigma = 0\%$ both KTO and NTO surface states are already separated from the CB by a total of $\Delta E = 0.08$ eV for the former and $\Delta E = 0.21$ eV for the latter, which characterizes them as shallow states within the bandgap. The planarity values of TaO_4 surface tetrahedra are $P_L = 77.4\%$ (KTO) and $P_L = 79.1\%$ (NTO). When the tensile limit of $\sigma = 4\%$ is achieved, such planarity rises to 80.7% and 81.5%, respectively. Accordingly, ΔE increases to 0.33 eV (KTO) and 0.30 eV (NTO), which sets the levels even further into the gap. On the other hand, when the compression limit of $\sigma = -4\%$ is reached, P_L of surface TaO_4 units reduces to 70.4% for KTO and 71.5% for NTO. This approximates surface states and the CB, resulting in a significant bands overlap for KTO, and reducing ΔE to 0.05 eV for NTO. The above results shall be explained in two different but complementary discussions: (i) the reason why surface Ta d states lie below the CB; (ii) the way biaxial strain changes the position of such states.

As for the first, we have to consider the consequences that cleaving atomic bonds triggers on an initially TaO_6 octahedral (O_h) symmetry existing in bulk KTO and NTO. As part of a group five transition metal, the five-fold degenerated Ta d orbitals are split by the ligand field of six oxygen atoms approaching along the axes, forming a set of doubly-degenerated e_g (d_{z^2} and $d_{x^2-y^2}$) and triple-degenerated t_{2g} (d_{xy}, d_{yz}, d_{zx}) orbitals. Being oxygen a π-donor ligand, charge transfer occurs through π bonds due to lateral overlap of ligand O 2p and Ta t_{2g} orbitals, which causes their energy to decrease. On the other hand, e_g orbitals rise in energy since their interactions with ligand orbitals are mostly repulsive (σ^*)[49]. Consequently, in the TaO_6 bulk arrangement, the CB is composed by Ta t_{2g}-Op (π^*) bands followed by a higher lying set of Ta e_g-O p (σ^*) bands. Cleaving the crystal in order to reduce

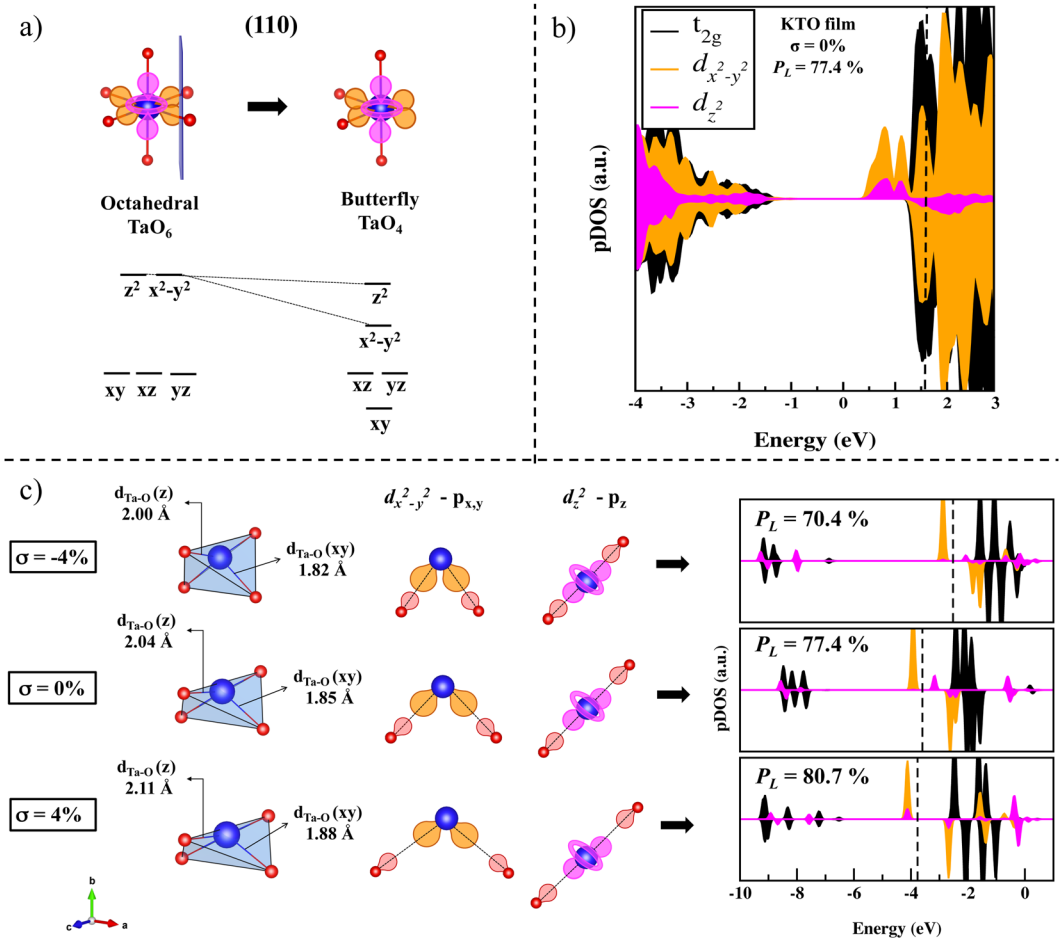

Figure 5. Investigation of individual TaO_4 units and their electronic characterization: (**a**) schematic representation of how the (110) cleavage removes *cis* oxygen ligands and stabilizes e_g orbitals; (**b**) relaxed strain-free ($\sigma = 0\%$) KTO film projected density of states on e_g and t_{2g} orbitals; (**c**) from the left to the right, structural changes such as the variation of both Ta-O bond distances and the unit planarity are induced by biaxial strain, which alters *d-p* repulsive interactions, and shift e_g states to lower (tensile, further stabilization) or higher (compression, destabilization) energy zones, as shown by the individual isolated TaO_4 pDOS. Red, orange, and pink schematic orbitals refer to O *p*, Ta $d_{x^2-y^2}$, and Ta d_{z^2} orbitals, respectively. Black dashed lines within pDOS plots represent the Fermi level.

the unit coordination to TaO_4 removes two oxygen ligands. In such cases, the absence of ligands along the axes stabilizes the corresponding e_g orbital, reducing their repulsive interactions[50]. Therefore, e_g orbitals shall lower in energy but now with the degeneracy broken since d_{z^2} and $d_{x^2-y^2}$ will not be equally stabilized. For instance, changes in the ligand field as it moves from octahedral to a square planar symmetry are generally described as a consequence of removing two ligands along the *z*-axis, which stabilizes d_{z^2} orbitals electrostatically and increases the energy of $d_{x^2-y^2}$ orbitals that now suffer the greatest repulsion[51] (Fig. 4S). For the proposed thin films, the (110) cleavage removes two *cis* oxygen atoms, leaving initially 'butterfly' TaO_4 complexes on the surface. Such a cleavage cut out half of $d_{x^2-y^2}$ interactions, while the main electrostatic repulsion in *z* remains the same, as illustrated in Fig. 5(a). The O-Ta-O angles may acquire variable values, changing the TaO_4 planarity so that tetrahedral (T_d), square planar (D_{4h}), and intermediate symmetries are allowed. In the studied structures, relaxation induces intermediate values of planarity to reach the structure equilibrium, balancing electrostatic and steric interactions. Figure 5(b) reveals the e_g nature of surface states near the CB, confirming the stabilization of $d_{x^2-y^2}$ orbitals caused by the (110) cleavage. The small contribution of d_{z^2} states result from a slight stabilization of its central lobe that reduces in energy when two weak antibonding interactions are removed.

As for the way that biaxial strain changes the position of surface Ta *d* states, an individual investigation of isolated TaO_4 units is required. We have calculated TaO_4 tetrahedral groups with different spatial arrangements in 20 Å vacuum supercells (oxygen atoms were saturated with hydrogen to mimic their coordination in both bulk and films). In addition to the configurational case of the strain-free KTO film, we have also calculated TaO_4 units with the coordinates and hence planarity in which they are found on KTO film surfaces when $\sigma = \pm 4\%$. In the left panel of Fig. 5(c), starting from the strain-free tetrahedra ($\sigma = 0\%$, $d_{TaO}(xy) = 1.85$ Å, and $d_{TaO}(z) = 2.04$ Å), it is shown that biaxial tensile ($\sigma = 4\%$) stretches $d_{Ta\text{-}O}$ bonds to $d_{TaO}(xy) = 1.88$ Å, and $d_{TaO}(z) = 2.11$ Å, rising the unit planarity, whereas biaxial compression ($\sigma = -4\%$) diminishes the atomic bond distances to $d_{TaO}(xy) = 1.82$ Å, and

$d_{TaO}(z) = 2.00$ Å, decreasing the planarity. All bond distances of the discussed cases can be found in Table 2S. The central panel of Fig. 5(c) illustrates the weakening or strengthening of repulsive interactions between antibonding Ta e_g-O *p* orbitals when tensile or compression is applied, respectively. The consequence in the material's electronic structure is depicted on the right panel. The projected density of states reveals that as a (110) cleavage is performed in the cubic bulk, $d_{x^2-y^2}$ and d_{z^2} states are stabilized and appear occupied (spin-up) below the Fermi level after structural relaxation. If biaxial tensile strain is applied in the *x*-*z* plane, Ta-O bonds will stretch, repulsive *d*-*p* interactions along such axes will decrease, and e_g orbitals are stabilized. Conversely, biaxial compression along *x*-*z* brings atoms close together, repulsive *d*-*p* interactions increase, and e_g orbitals rise in energy.

Finally, we note the fact that the electronic structure of ultrathin KTO films appears to be more sensitive to changes in surface TaO_4 planarity than NTO films. As shown in Fig. 4 (left *y*-axis), the planarity of superficial TaO_4 groups in both films respond very similarly to biaxial strain. Showing an essentially linear variation, the P_L increases under tensile and decreases under compression, following basically the same slope. On the other hand, the linear coefficient is smaller for the KTO film than for the NTO one, what indicates that the initial planarity of the former is intrinsically lower than that of the latter. Since potassium has an extra electron shell compared to sodium, and hence a larger atomic radius, the repulsion felt by the superficial K-Ta-O arrangement is greater than in the case of Na-Ta-O, which initially prevents KTO-TaO_4 groups from being as planar as NTO-TaO_4 ones. As the electrostatic interactions are stronger for KTO, it was expected that its electronic structure would change more sensibly upon strain, as shown in Fig. 2. The exact influence of A-site cation on this type of process is still under investigation, nevertheless.

We also suggest that there are upper and lower limits of planarity that biaxial strain is able to induce. Despite the almost linear behavior of P_L as a function of strain, too high tensile values stretch Ta-O to such an extent that the TaO_4 coordination might be broken. In turn, too high compressive values maximize electrostatic and steric repulsions. For the KTO film, for instance, the repulsion at $\sigma = -4\%$ is such that potassium atoms start a exsolution-like process and are "expelled" from the surface of the film, TaO_4 planarity values decrease drastically, and the electronic structure changes considerably. When the maximum tensile is achieved, in turn, both films tend to the similar planarity values and to the same ΔE maximum of ~0.30 eV from which greater P_L is only achieved if more severe strain that irreversibly destabilizes the system is applied.

Conclusions

In conclusion, the (110) cleavage in cubic $KTaO_3$ and $NaTaO_3$ crystals made to obtain ultrathin films modifies the Ta *d* orbitals degeneracy and local electrostatic interactions to such an extent that shallow surface states can be manipulated by biaxial strain. Cleaving the crystal in such direction naturally induces $d_{x^2-y^2}$ orbitals stabilization and introduces them near the CB. We systematically investigated and showed that biaxial tensile or compression modifies surface TaO_4 planarity, and therefore the energy of electronic defect states. Biaxial tensile pushes them further into the material's bandgap while compression moves them towards the CB. As the behavior is generically the same for both different tantalates, we report a practical way of tuning their electronic properties through biaxial strain. Our results elucidate meaningful structural-electronic relationships that can be readily harnessed to control and engineer bandgap energy states. Although further investigation is required to connect such results with tactile applications, the proposed engineering may be widely desirable. For photocatalysis (the main application of $NaTaO_3$ nanostructures), for instance, the alignment of CB and VB states with the water redox potentials is a major challenge and usually achieved by doping. Such strain-driven modulation may be effective and rule out the use of foreign materials. Concerning less explored applications, as spintronics, the magnetic characteristics of the system can be useful for building spin filters or similar devices.

Received: 8 January 2020; Accepted: 6 April 2020;
Published online: 08 May 2020

References

1. Li, C., Soh, K. C. K. & Wu, P. Formability of abo3 perovskites. *Journal of alloys and compounds* **372**, 40–48 (2004).
2. Bhalla, A., Guo, R. & Roy, R. The perovskite structure - a review of its role in ceramic science and technology. *Materials research innovations* **4**, 3–26 (2000).
3. Emery, A. A. & Wolverton, C. High-throughput dft calculations of formation energy, stability and oxygen vacancy formation energy of abo 3 perovskites. *Scientific data* **4**, 170153 (2017).
4. Du, H., Jia, C.-L. & Mayer, J. Surface atomic structure and growth mechanism of {100}-faceted perovskite oxide nanocubes. In *European Microscopy Congress 2016: Proceedings*, 201–202 (Wiley Online Library, 2016).
5. Huang, K., Yuan, L. & Feng, S. Crystal facet tailoring arts in perovskite oxides. *Inorganic Chemistry Frontiers* **2**, 965–981 (2015).
6. Liu, G., Jimmy, C. Y., Lu, G. Q. M. & Cheng, H.-M. Crystal facet engineering of semiconductor photocatalysts: motivations, advances and unique properties. *Chemical Communications* **47**, 6763–6783 (2011).
7. Wang, S., Liu, G. & Wang, L. Crystal facet engineering of photoelectrodes for photoelectrochemical water splitting. *Chemical reviews* **119**, 5192–5247 (2019).
8. May, S. *et al*. Quantifying octahedral rotations in strained perovskite oxide films. *Physical Review B* **82**, 014110 (2010).
9. Vailionis, A. *et al*. Misfit strain accommodation in epitaxial a b o 3 perovskites: Lattice rotations and lattice modulations. *Physical Review B* **83**, 064101 (2011).
10. Balachandran, P. V. & Rondinelli, J. M. Interplay of octahedral rotations and breathing distortions in charge-ordering perovskite oxides. *Physical Review B* **88**, 054101 (2013).
11. Rondinelli, J. M. & Fennie, C. J. Octahedral rotation-induced ferroelectricity in cation ordered perovskites. *Advanced Materials* **24**, 1961–1968 (2012).
12. Kato, H., Matsudo, N. & Kudo, A. Photophysical and photocatalytic properties of molybdates and tungstates with a scheelite structure. *Chemistry letters* **33**, 1216–1217 (2004).
13. Portugal, G. R., Santos, S. F. & Arantes, J. T. Natao3 cubic and orthorhombic surfaces: An intrinsic improvement of photocatalytic properties. *Applied Surface Science* **502**, 144206 (2020).

14. Wang, Y. *et al*. Hydrothermal growths, optical features and first-principles calculations of sillenite-type crystals comprising discrete mo 4 tetrahedra. *CrystEngComm* **14**, 1063–1068 (2012).
15. Zahedi, E., Xiao, B. & Shayestefar, M. First-principles investigations of the structure, electronic, and optical properties of mullite-type orthorhombic bi2m4o9 (m= al3+, ga3+). *Inorganic chemistry* **55**, 4824–4835 (2016).
16. Fujiwara, T. *et al*. Heteroepitaxial barium-doped natao3 films on srtio3 (001) substrate. *Thin Solid Films* **658**, 66–72 (2018).
17. Haeni, J. *et al*. Room-temperature ferroelectricity in strained srtio 3. *Nature* **430**, 758 (2004).
18. Pai, Y.-Y., Tylan-Tyler, A., Irvin, P. & Levy, J. Physics of srtio3-based heterostructures and nanostructures: a review. *Reports on Progress in Physics* **81**, 036503 (2018).
19. Tagantsev, A., Pertsev, N., Muralt, P. & Setter, N. Strain-induced diffuse dielectric anomaly and critical point in perovskite ferroelectric thin films. *Physical Review B* **65**, 012104 (2001).
20. Lloyd, D. *et al*. Band gap engineering with ultralarge biaxial strains in suspended monolayer mos2. *Nano letters* **16**, 5836–5841 (2016).
21. Lin, Z. *et al*. Quasi-two-dimensional superconductivity in fese 0.3 te 0.7 thin films and electric-field modulation of superconducting transition. *Scientific reports* **5**, 1–9 (2015).
22. Trommler, S. *et al*. Reversible shift in the superconducting transition for la1. 85sr0. 15cuo4 and bafe1. 8co0. 2as2 using piezoelectric substrates. *New Journal of Physics* **12**, 103030 (2010).
23. Lee, Y. *et al*. Preparation and characterization of sodium tantalate thin films by hydrothermal-electrochemical synthesis. *Chemistry of materials* **17**, 2422–2426 (2005).
24. Polak, L. *et al*. Two-step sputter-hydrothermal synthesis of natao3 thin films. *Thin Solid Films* **603**, 413–417 (2016).
25. Zhou, X., Chen, Y., Mei, H., Hu, Z. & Fan, Y. A facile route for the preparation of morphology-controlled $natao_3$ films. *Applied Surface Science* **255**, 2803–2807 (2008).
26. Goh, G. K., Levi, C. G. & Lange, F. F. Hydrothermal epitaxy of ktao 3 thin films. *Journal of Materials Research* **17**, 2852–2858 (2002).
27. Skoromets, V. *et al*. Ferroelectric phase transition in polycrystalline ktao3 thin film revealed by terahertz spectroscopy. *Applied Physics Letters* **99**, 052908 (2011).
28. Narkilahti, J. & Tyunina, M. The structure of strained perovskite ktao3 thin films prepared by pulsed laser deposition. *Journal of Physics: Condensed Matter* **24**, 325901 (2012).
29. Tyunina, M. *et al*. Ultrathin srtio3 films: epitaxy and optical properties. *Journal of Physics: Condensed Matter* **21**, 232203 (2009).
30. May, S., Santos, T. & Bhattacharya, A. Onset of metallic behavior in strained (lanio 3) n/(srmno 3) 2 superlattices. *Physical Review B* **79**, 115127 (2009).
31. Son, J., LeBeau, J. M., Allen, S. J. & Stemmer, S. Conductivity enhancement of ultrathin lanio 3 films in superlattices. *Applied Physics Letters* **97**, 202109 (2010).
32. Scherwitzl, R., Zubko, P., Lichtensteiger, C. & Triscone, J.-M. Electric-field tuning of the metal-insulator transition in ultrathin films of lanio 3. *Applied Physics Letters* **95**, 222114 (2009).
33. Lee, M. K., Nath, T. K., Eom, C.-B., Smoak, M. C. & Tsui, F. Strain modification of epitaxial perovskite oxide thin films using structural transitions of ferroelectric batio 3 substrate. *Applied Physics Letters* **77**, 3547–3549 (2000).
34. Gan, Q., Rao, R., Eom, C., Garrett, J. & Lee, M. Direct measurement of strain effects on magnetic and electrical properties of epitaxial srruo 3 thin films. *Applied Physics Letters* **72**, 978–980 (1998).
35. Rotella, H. *et al*. Octahedral tilting in strained lavo 3 thin films. *Physical Review B* **85**, 184101 (2012).
36. Wu, Z. *et al*. Effect of biaxial strain induced by piezoelectric pmn-pt on the upconversion photoluminescence of batio 3: Yb/er thin films. *Optics express* **22**, 29014–29019 (2014).
37. Hohenberg, P. & Kohn, W. Inhomogeneous electron gas. *Physical review* **136**, B864 (1964).
38. Kohn, W. & Sham, L. J. Self-consistent equations including exchange and correlation effects. *Physical review* **140**, A1133 (1965).
39. Kresse, G. & Furthmüller, J. Efficient iterative schemes for ab initio total-energy calculations using a plane-wave basis set. *Physical review B* **54**, 11169 (1996).
40. Kresse, G. & Joubert, D. From ultrasoft pseudopotentials to the projector augmented-wave method. *Physical Review B* **59**, 1758 (1999).
41. Blöchl, P. E. Projector augmented-wave method. *Physical review B* **50**, 17953 (1994).
42. Perdew, J. P., Burke, K. & Ernzerhof, M. Generalized gradient approximation made simple. *Physical review letters* **77**, 3865 (1996).
43. Monkhorst, H. J. & Pack, J. D. Special points for brillouin-zone integrations. *Physical review B* **13**, 5188 (1976).
44. Kato, H. & Kudo, A. Water splitting into h2 and o2 on alkali tantalate photocatalysts atao3 (a= li, na, and k). *The Journal of Physical Chemistry B* **105**, 4285–4292 (2001).
45. Lee, K., Choi, J., Lee, J. & Baik, S. Domain formation in epitaxial pb (zr, ti) o 3 thin films. *Journal of Applied Physics* **90**, 4095–4102 (2001).
46. Modak, B., Srinivasu, K. & Ghosh, S. K. Band gap engineering of natao 3 using density functional theory: a charge compensated codoping strategy. *Physical Chemistry Chemical Physics* **16**, 17116–17124 (2014).
47. Bouafia, H. *et al*. Structural, elastic, electronic and thermodynamic properties of ktao3 and natao3: Ab initio investigations. *Computational Materials Science* **75**, 1–8 (2013).
48. Li, Z., Chen, G. & Liu, J. Electron structure and optical absorption properties of cubic and orthorhombic natao3 by density functional theory. *Solid state communications* **143**, 295–299 (2007).
49. Albright, T. A., Burdett, J. K. &Whangbo, M.-H. *Orbital interactions in chemistry* (John Wiley & Sons, 2013).
50. Parida, P., Kashikar, R., Jena, A. & Nanda, B. Universality in the electronic structure of 3d transition metal oxides. *Journal of Physics and Chemistry of Solids* **123**, 133–149 (2018).
51. Jean, Y. *Molecular orbitals of transition metal complexes* (OUP Oxford, 2005).

Acknowledgements

We acknowledge the Brazilian agency CAPES and FAPESP (2017/02317-2) for financial support. We also thank UFABC and "Centro Nacional de Processamento de Alto Desempenho em Campinas - São Paulo (CENAPAD-Campinas, SP)" for the computational facilities.

Author contributions

J.T. Arantes and G.R. Portugal contributed equally to this work. All authors reviewed the manuscript.

Competing interests

The authors declare no competing interests.

Additional information

Supplementary information is available for this paper at https://doi.org/10.1038/s41598-020-64315-7.

Correspondence and requests for materials should be addressed to J.T.A.